Journal of Materials Chemistry A

Accepted Manuscript

ROYAL SOCIETY OF CHEMISTRY

www.rsc.org/materialsA

Journal of Material Chemical A

RSCPublishing

ARTICLE

Atomically Thin $MoSe_2$/graphene and WSe_2/graphene Nanosheets for Highly Efficient Oxygen Reduction Reaction

Cite this: DOI: 10.1039/x0xx00000x

Received 00th January 2012,
Accepted 00th January 2012

DOI: 10.1039/x0xx00000x

www.rsc.org/

Jiahao Guo,[a,b] Yantao Shi,[a,]* Xiaogong Bai,[a] Xuchun Wang,[b] and Tingli Ma [c,d]*

As a conceptually new class of 2D materials, inorganic graphene analogues (IGAs) ultrathin nanosheets perform an increasingly vital function in various electronic devices. However, the relatively low electrical conductivity of IGAs ultrathin nanosheets severely hampers their application as electrode materials in devices. Through in-situ synthesis, we report the combination of inorganic graphene and graphene into atomically thin nanosheets as efficient electrocatalysts for oxygen reduction reaction (ORR). Benefitting from the advantages of both IGAs and reduced graphene oxide, the g–$MoSe_2$ and g–WSe_2 nanocomposites showed excellent ORR activity associated with a number of exchanged electrons close to four, which corresponded to the complete reduction of oxygen into water. In specific, the two electrocatalysts exhibited a positive onset potential of -0.02 V (close to that of Pt/C, 0.02 V) and a high kinetic current density (J_K) of 10.22 mA·cm^{-2} for g–$MoSe_2$ and 10.77 mA·cm^{-2} for g–WSe_2 at –0.20 V. Compared with commercial Pt/C, these catalysts possess outstanding long-term durability and fuel crossover resistance capacity in alkaline media. Therefore, nanocomposites of inorganic graphene and graphene can be developed into low-cost and efficient alternatives (to the noble metal Pt) to serve as cathodic electrode in fuel cells.

1. Introduction

Heterogeneous electrocatalytic reactions usually involve reactant adsorption, product desorption, and charge-transfer processes on the surface of solid catalysts.[1,2] Therefore, catalyst with excellent performance must possess a large surface area, good electrical conductivity, and good durability. Oxygen reduction reaction (ORR) is a heterogeneous electrocatalytic reaction important in energy conversion applications, including fuel cells and metal–air batteries.[3,4] Pt-based materials are active ORR electrocatalysts, but their large-scale applications are limited by the scarcity, prohibitive cost, and limited durability of noble metals.[5–7] Therefore, the development of non-Pt catalysts with low cost, competitive catalytic activity, and durability has become an urgent need to promote the industrialization of fuel cells.[8,9]

Ultrathin nanosheets of 2D materials such as graphene and inorganic graphene analogues (IGAs) have attracted considerable attention in recent years because of their unique physical and chemical properties that allow their incorporation into nanoelectronic devices and energy storage devices.[10–12] 2D layered materials exhibit high anisotropy in material properties because of the large difference between intra- and interlayer bonding. This feature presents opportunities to engineer materials whose properties strongly depend on the orientation of the layers relative to the substrate. These materials often possess large surface areas and contain large amounts of coordination-unsaturated surface atoms, which promote the adsorption of reactants and thus improve catalytic properties.[13] For example, as a typical IGAs, MoS_2 has widely used in gas storage, super capacitor, lithium ion battery, ORR, and sensor, and achieved good results.[14] The single-crystal monolayer and multilayer graphene acquired by different methods exhibits remarkably high conductivity and large surface area.[15–18] This feature makes it suitable for the carrier of electrocatalysts and drawn much interest.[19-22] However, as another conceptually new class of 2D materials, IGAs remain to have limited applications as highly conductive electrodes; in particular, common IGAs are semiconducting or insulating ($MoSe_2$ and WSe_2).[23] Selenides demonstrate unsatisfactory performance as ORR catalysts because of their low conductivity.[24–26] As typical IGAs, $MoSe_2$ and WSe_2 on carbon fiber paper display excellent catalytic activities in hydrogen evolution reaction.[27] As a 2D carbon material with favorable conductivity, graphene is an ideal substrate to combine with IGAs to form highly efficient electrocatalysts that can improve the conductivity of IGAs and produce strong interactions between IGAs and graphene.

In this study, we report the successful synthesis of atomically thin $MoSe_2$/reduced graphene oxide (g–$MoSe_2$) and WSe_2/reduced graphene oxide (g–WSe_2) nanosheets through a reductant–free and

insitu solvothermal route for high-performance ORR electrocatalysts. The two nanocomposites possessed mesoporous structures that facilitate oxygen adsorption and moss transport during the ORR. The catalytic activity of g–$MoSe_2$ and g–WSe_2 was compared with those of individual $MoSe_2$ and WSe_2 nanosheets and commercial Pt/C. Compared with those of individual $MoSe_2$ and WSe_2, the catalytic performance of the two nanocomposites for ORR was considerably improved, closely approximating that of commercial Pt/C in both the reaction current and the initial potential. Notably, the two nanocomposites exhibited higher tolerance against fuel crossover and stronger durability in alkaline media compared with the vulnerable commercial Pt/C.

2. Experimental

2.1 Preparation of atomically thin g–$MoSe_2$ and g–WSe_2 single-layer nanosheets

Ultrasonic exfoliation of graphene oxide (GO):[28] Graphene oxide (300mg), deionized water (125 mL), and anhydrous ethanol (125 mL) were added into a 500 mL flask. The flask was sealed and sonicated at a low-power sonic bath (KQ3200DA) for 12 h. The resultant dispersions were centrifuged at 600 rpm for 30 min, and then the supernatant was collected. After the supernatant was centrifuged at 12,000 rpm for 15 min, the as-obtained products were collected, washed with deionized water and anhydrous ethanol for multiple times, and then dried under vacuum overnight for further characterization.

Synthesis of atomically thin g–$MoSe_2$ and g–WSe_2 single-layer nanosheets: In a typical procedure,[29] 17 mg of exfoliated GO, 2 mmol of WCl_6 (or $MoCl_5$), and 4 mmol of Se powder were mixed and added into 40 mL of degassed (with N_2) oleylamine at room temperature. After continuous stirring for 5 min, the reaction mixture was transferred into a three-neck round-bottom flask, sealed, and then degassed in high-purity N_2 atmosphere for 10 min under magnetic stirring. Then, the mixture was heated up to 280 °C and allowed to be reacted for 4 h at the same temperature in N_2 atmosphere with vigorous agitation. Finally, the mixture was cooled gradually to room temperature with at ~5 °C·min^{-1}. The black products that precipitated at the bottom of the flask were obtained. Large amounts of hexane were then added into the crude solution, and the products were isolated via centrifugation repeatedly, dried under vacuum, and heated at 450 °C for 3h in N_2 atmosphere.

Synthesis of selenides: The synthesis procedure of selenides is the same as those of g–$MoSe_2$ and g–WSe_2, except exfoliated GO was not added.

2.2 Materials characterization

X-ray powder diffraction (XRD) patterns were recorded on a Rigaku D/max–rA X-ray diffractometer with Cu Kα radiation (λ = 1.54178 Å). Field emission scanning electron microscopy (FESEM) images were obtained using a FEI HITACHI S–4800 FESEM instrument. Transmission electron microscopy (TEM) images, high-resolution TEM (HRTEM) images, and selected-area electron diffraction (SAED) patterns were obtained using a JEOL–2010 TEM with an acceleration voltage of 200 kV. X-ray photoelectron spectroscopy (XPS) were acquired on an ESCALAB MKII X–ray photoelectron spectrometer with Mg Kα ($h\upsilon$ = 1253.6 eV) as the excitation source. Atomic force microscopy (AFM) was performed using the Veeco DI Nano-scope MultiMode V system. Nitrogen adsorption isotherms were collected on a Tristar II 3020 Micromeritics adsorption analyzer at 77 K. Prior to adsorption measurements, the samples were degassed at 200 °C for a minimum of 10 h. Pore size distribution (PSD) was calculated by using the adsorption branch of the isotherms through the Barrett–Joyner–Halenda method. The total pore volume was estimated from the adsorption volume at a relative pressure (P/P_0) of 0.99.

2.3 Electrochemical measurements

The catalyst was redispersed in a mixture of solvents containing deionized water, isopropanol, and Nafion (5%) solution (v/v/v= 2.5:1:0.06) to form a 4 mg·mL^{-1} suspension, and the mixture was ultrasonicated for approximately 1 h to form a homogeneous ink. Pt/C ink was prepared by dispersing 4 mg of Pt/C (20 wt% Pt on Vulcan XC–72) in 1 mL of ethanol with 35 μL of 5 wt% Nafion solution. A glassy carbon (GC) disk electrode (PINE, 5 mm diameter, 0.196 cm^2) served as support. Prior to use, the GC electrode was polished to a mirror finish and thoroughly cleaned. The catalyst ink (5 μL) was casted on the electrode and dried under ambient conditions to yield a catalyst loading of ~100 μg·cm^{-2}.

Electrocatalytic activity was evaluated via cyclic voltammetry (CV) and the rotating disk electrode (RDE) technique. Electrochemical measurements were performed in a standard three-electrode glass cell on a CHI 660C electrochemical workstation (Chenhua, Shanghai) under ambient conditions. The modified GC electrode, a Pt plate, and Ag/AgCl (PINE, 4 M KCl) were used as the working, counter, and reference electrodes, respectively. KOH aqueous solution (0.1 M) was employed as the electrolyte. Before testing, O_2/N_2 flow was passed through the electrolyte in the cell for 30 min to saturate it with O_2/N_2. CV tests were conducted from 0.2 V to −1.0 V versus Ag/AgCl (PINE, 4 M KCl) at a sweep rate of 10 mV·s^{-1}. The working electrode was cycled at least 10 times before data were recorded. Long-term durability and methanol crossover tests were also conducted on nanocomposite catalysts and Pt/C by using the same setup as in CV with O_2 continuous flow. The RDE measurements of the different catalysts were conducted in O_2-saturated KOH solution at a scan rate of 10 mV·s^{-1} and various rotation speeds from 400rmp to 2500 rpm.

The overall electron transfer numbers per oxygen molecule involved in the typical ORR process were calculated from the slopes of the Koutecky–Levich (K-L) plots by using the following equations:[30–32]

$$\frac{1}{j} = \frac{1}{j_k} + \frac{1}{B\omega^{1/2}} \quad (1)$$

Where j is the measured current density, j_K is the kinetic current density, and ω is the electrode rotation speed in rmp. B was determined from the slope of K–L plots on the basis of the Levich equation as provided below:

$$B = 0.2nF\left(D_{O_2}\right)^{2/3}\nu^{-1/6}c_{O_2} \quad (2)$$

where n is the number of electrons transferred per oxygen molecule, F is the Faraday constant (F = 96 485 C·mol^{-1}), D_{O_2} is the diffusion coefficient of O_2, c_{O_2} is the bulk concentration of O_2, and ν is the kinetic viscosity of the electrolyte. In this study, the electrolyte was O_2-saturated 0.1 M KOH. The D_{O_2}, c_{O_2}, and ν values used were 1.9×10^{-5} $cm^2\cdot s^{-1}$, 1.2×10^{-6} mol·cm^{-3}, and 0.01 $cm^2\cdot s^{-1}$, respectively.

The constant 0.2 in Equation 2 is adopted when the rotation speed is expressed in rpm.

3. Results and discussion

3.1 Material characterization

The structure and morphology of the composite materials were examined. The SEM images of $MoSe_2$, g–$MoSe_2$, WSe_2, and g–WSe_2 are shown in Figure S1. As shown in Figure S1a, $MoSe_2$ is composed of interlaced and ultrathin nanosheets. The $MoSe_2$ nanosheets are approximately 10 nm thick with typical lateral dimensions between 100 and 150 nm. The morphology of the nanocomposite did not change after combination with the reduced graphene oxide (rGO) (Figure S1b). WSe_2 is composed of twisted and ultrathin nanoplates with an average thickness of approximately 10 nm and width of 80–150 nm. The g–WSe_2 nanocomposite presents an irregular plate morphology (Figure S1d). The TEM images of the four materials are shown in Figures 1 and S2. $MoSe_2$ shows interconnected nanosheets, whereas WSe_2 features twisted nanoplates. The HRTEM images of $MoSe_2$ and WSe_2 (Figures S2b and S2d) show lattice fringes with spacing of 0.283 and 0.281 nm, which correspond to the (100) and (100) planes of hexagonal $MoSe_2$ and WSe_2, respectively. The TEM images of g–$MoSe_2$ and g–WSe_2 in Figures 1a and 1d show that the $MoSe_2$ nanosheets and WSe_2 nanoplates are uniformly distributed on the surfaces of the rGO sheets. Moreover neighboring single $MoSe_2$ nanosheets and WSe_2 nanoplates are occasionally agglomerated during their growth. The HRTEM images of g–$MoSe_2$ and g–WSe_2 (Figures 1b and 1e) similarly show lattice fringes with spacing of 0.283 and 0.281 nm, which correspond to the (100) and (100) planes of hexagonal $MoSe_2$ and WSe_2, respectively. The white lines marked in Figures 1b and 1e are the lattice fringes of the $MoSe_2$ and WSe_2 nanosheets. The SAED patterns in Figures 1b and 1e reveal *d*-spacing values of ~0.28, 0.25, 0.20, and 0.16 nm corresponding to the (100), (103), (105), and (110) planes of 2H-$MoSe_2$ and WSe_2, respectively. These values agree with the *d*-spacing values of bulk $MoSe_2$ and WSe_2.[33] Previous reports[34,35] revealed that AFM can be used to identify whether or not graphene is single layered or multilayered. AFM images and the corresponding height profiles are shown in Figures 1c, 1f, and S3. In Figure S3, AFM clearly shows that the relatively irregular, smooth

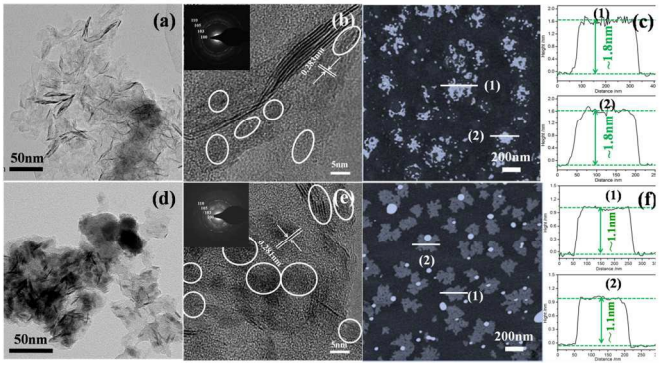

Figure 1 (a, b) TEM and HRTEM images of g–$MoSe_2$. The inset in (b) shows the corresponding SAED pattern. (c) AFM image and height profiles from sections as indicated by the white lines of g–$MoSe_2$. (d, e) TEM and HRTEM images of g–WSe_2. The inset in (d) shows the corresponding SAED pattern. (f) AFM image and height profiles from sections as indicated by the white lines of g–WSe_2.

2D sheet structures possess an average height of approximately 0.7 nm for $MoSe_2$ and WSe_2. This finding agrees with the crystallography data of $MoSe_2$ and WSe_2 in the literature, indicating that $MoSe_2$ and WSe_2 possess single-layer structures.[36,37] The average sheet height for g–$MoSe_2$ is approximately 1.8 nm, suggesting that the structure is composed of a single layer of graphene and two layers of $MoSe_2$. Meanwhile, the average height of the g–WSe_2 sheet is approximately 1.1 nm, indicating that the sheet is composed of a single layer of graphene and a layer of WSe_2. This layer-by-layer structure is beneficial to the improvement of electrical conductivity, providing easy transfer charge ability as an electrode. In addition, this layered nanostructure facilitates reactant adsorption and improves the reactive sites, resulting in excellent catalytic activity.

The XRD patterns of the four samples are shown in Figures 2 and S2. For the WSe_2 and g–WSe_2 samples, the diffraction peaks at 13.60°, 27.70°, 31.92°, 37.82°, 41.54°, 47.34°, 56.42°, and 66.34° are assigned to the (002), (004), (100), (103), (006), (105), (008), and (108) crystal planes, respectively (38-1388, PDF 2 database). For the $MoSe_2$ and g–$MoSe_2$ samples, the diffraction peaks at 13.70°, 27.58°, 31.56°, 37.68°, 41.80°, 47.68°, 56.16°, and 66.74° are assigned to the crystal planes of (002), (004), (100), (103), (006), (105), (008), and (108), respectively (29-0914, PDF 2 database). These results indicate that the hexagonal $MoSe_2$ and WSe_2 were successfully synthesized. The lattice parameters are as follows: *a* =3.287 Å and *c* =12.925 Å for $MoSe_2$, and *a* =3.286 Å and *c* =12.983 Å for WSe_2. These values indicate that the crystal structures are almost similar. For rGO, a diffraction peak should exist at 13.44°.[38] However, the diffraction peaks of rGO for the g–WSe_2 and g–$MoSe_2$ samples are masked by the overlap in diffraction peaks at about 13.60° of WSe_2 and $MoSe_2$.

Nitrogen adsorption isotherms were measured to investigate the pore structure of the four as-prepared materials. The isotherms of $MoSe_2$, WSe_2, and g–$MoSe_2$ are type–IV and g–WSe_2 is type-□ with a distinct hysteresis loop at relative pressures (P/P_0) from 0.45 to 1.0 (Figure 3a), suggesting the presence of mesopores in these materials. The PSD curves of $MoSe_2$ and g–$MoSe_2$ are both centered at approximately 30 nm whereas that of WSe_2 is centered at approximately 42 nm, which is larger than that of g–WSe_2 (≈23 nm) (Figure 3b). The PSD results further confirm the mesoporous

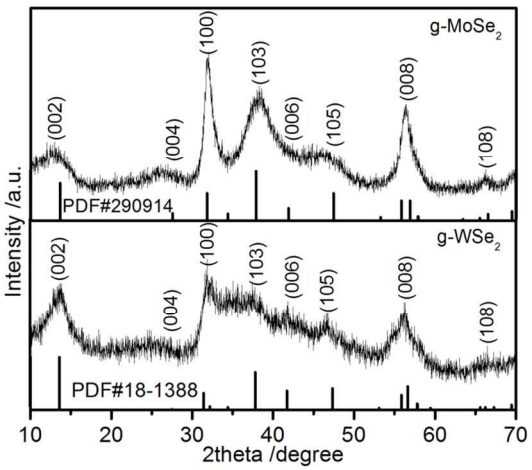

Figure 2 XRD patterns of the g–WSe_2 and g–$MoSe_2$ composite catalysts.

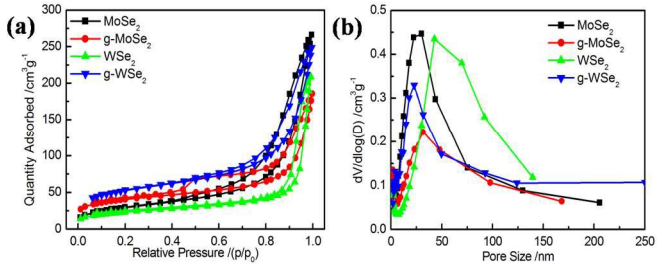

Figure 3 (a) Nitrogen adsorption–desorption isotherms and (b) pore size distribution curves of $MoSe_2$, g–$MoSe_2$, WSe_2, and g–WSe_2.

structure of the four materials. The Brunauer–Emmett–Teller surface area and the total pore volume were estimated to be 133.77 $m^2 \cdot g^{-1}$ and 0.25 $cm^3 \cdot g^{-1}$ for g–$MoSe_2$, 104.43 $m^2 \cdot g^{-1}$ and 0.41 $cm^3 \cdot g^{-1}$ for $MoSe_2$, 182.78 $m^2 \cdot g^{-1}$ and 0.37 $cm^3 \cdot g^{-1}$ for g–WSe_2, and 78.86 $m^2 \cdot g^{-1}$ and 0.33 $cm^3 \cdot g^{-1}$ for WSe_2, respectively. This result suggests that the surface areas of the nanocomposites are enlarged, which increase the number of active sites and produce unprecedented catalytic properties. Conversely, the mesoporous structure of the four materials similarly facilitates oxygen adsorption and molecular transport during the ORR.

To detect the strong interaction between two components in the composite electrocatalyst, Raman spectroscopy measurements were conducted. Figure 4 shows the Raman spectra of GO, rGO, g-$MoSe_2$, and g-WSe_2. The Raman spectrum of GO displays a broad D band peak at 1365 cm^{-1}, G band peak at 1596 cm^{-1}, and combination peak of D+G band at 2900 cm^{-1}. For pure g-$MoSe_2$ and g-WSe_2, the two bands exhibit red-shift to about 1351 and 1587 cm^{-1}, respectively, suggesting an interaction between rGO and the selenide nanosheets. This interaction is conducive to promoting the stability of the catalyst interface, endowing the nanocomposites high stability. The Raman spectra of the nanocomposites also display signals of Mo–Se band (240 cm^{-1}) from g-$MoSe_2$ and W–Se band (250 cm^{-1}) from g-WSe_2. Compared with GO, the I_D/I_G values of rGO, g-$MoSe_2$ and g-WSe_2 increase, suggesting that GO had been reduced after reaction. Furthermore, the I_D/I_G values of g-$MoSe_2$ and g-WSe_2 are higher than that of rGO, which indicates the lower overlapping degree of g-$MoSe_2$ and g-WSe_2nanosheets (as graphitic evolution).

The surface elemental composition of the g–$MoSe_2$ and g–WSe_2 composites was further investigated via XPS. The full-range XPS spectra of g–$MoSe_2$, g–WSe_2, and GO are shown in Figure S5. The survey XPS spectra indicate the presence of Mo, Se, C, and O for g–

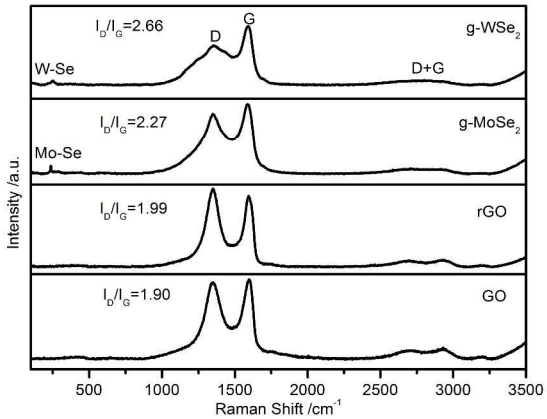

Figure 4 Raman spectra of GO, rGO, g-$MoSe_2$, and g-WSe_2.

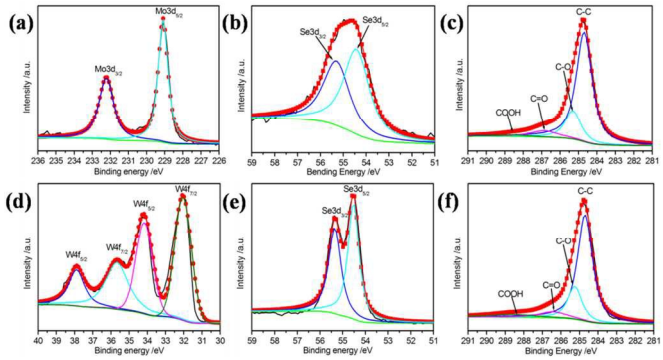

Figure 5 (a, d) High-resolution XPS spectra and corresponding deconvoluted spectra of Mo 3*d* of g–$MoSe_2$ and W 4*f* of g–WSe_2; (b, e) high-resolution XPS spectra and corresponding deconvoluted spectra of Se 3*d* of g–$MoSe_2$ and g–WSe_2; (c, f) C 1*s* core-level and corresponding deconvoluted spectra for the g–$MoSe_2$ and g–WSe_2 composites.

$MoSe_2$ and the presence of W, Se, C, and O for g–WSe_2, but only C and O can be detected for GO on the basis of binding energy. The deconvolution of the corresponding O 1s spectra (Figure S6) for the two composites indicates that at least two chemical bonding states, such as O2f and O3f, are on the surface.[39] The binding energies of Mo $3d_{5/2}$ and Mo $3d_{3/2}$ are 229.1 and 232.2 eV in Figure 5a, respectively, revealing the +4 oxidation chemical state of Mo.[40-43] As shown in Figures 5b and 5e, Se $3d_{5/2}$ and Se $3d_{3/2}$ respectively located at 54.5 and 55.3 eV appear around the same peak positions for both g–$MoSe_2$ and g–WSe_2. This finding indicates the same oxidation state of −2 for Se in both materials.[44,45] The peaks of W $4f_{7/2}$ and W $4f_{5/2}$ respectively located at 32.1 and 34.2 eV correspond to the +4 oxidation chemical state of W, and this finding agrees with a previous report on WSe_2.[42] The peaks at approximately 37.9 and 35.7 eV in Figure 5d are assigned to W $4f_{5/2}$ and W$4f_{7/2}$, which can be attributed to the +6 oxidation state of surface W.[39] Figure S5b shows the core-level XPS spectrum of C 1s and the corresponding deconvoluted spectra for GO sheets. The spectrum can be fitted with four components of oxygen-containing functional groups: (a) non-oxygenated C at 284.7 eV, (b) carbon in C–O at 286.8 eV, (c) epoxy carbon at 287.9 eV, and (d) carbonyl carbon at 289.0 eV.[46–48] Meanwhile, for the g–$MoSe_2$ and g–WSe_2 nanocomposites, the C1s spectrum becomes a major peak at 284.7 eV, and peaks corresponding to the C–O, C=O, and COOH bonds are obviously weakened. These findings suggest the effective reduction of GO sheets (Figures 5c and 5f). For the g–$MoSe_2$ and g–WSe_2 nanocomposites, the binding energy of the C–O bond located at 285.4 eV indicates the presence of a small amount of oxygen-containing carbon groups in the final nanocomposite. This phenomenon is commonly found for chemically rGO.[49] Basing from the devonvoluted XPS spectra of the C 1s peak, we calculated the percentages of different groups in the GO, g–$MoSe_2$, and g–WSe_2 nanocomposites (Table S1). Compared with that of GO, the fraction of C–C bonds increased from 32.9 % to 72.3 % for g–$MoSe_2$ and to 68.1% for g–WSe_2. Meanwhile, the fraction of C–O bonds significantly decreased from 53.2 % to 18.6 % for g–$MoSe_2$ and to 19.8% for g–WSe_2. These results suggest that the GO sheet was effectively reduced after the synthesis of selenides, which could be beneficial for firm combination. The fraction of COOH bonds for g–WSe_2 is significantly higher than that of g–$MoSe_2$, and this

difference can be related to the presence of the +6 oxidation state on the surface of g–WSe_2.

3.2 Electrocatalytic analysis

To gain insights into the ORR activities of g–$MoSe_2$ and g–WSe_2, we conducted CV measurements in 0.1 M KOH solution (Figures 6 and S7). Commercial Pt/C was also studied as a control experiment. All five electrodes, including $MoSe_2$, WSe_2, g–$MoSe_2$, g–WSe_2, and commercial Pt/C loaded on a glassy carbon disk electrode, show substantial reduction currents in the presence of O_2 (red line), whereas no obvious response can be observed under N_2 (black line). This result indicates that the cathodic currents at these electrodes originate from the ORR. The typical CV curve of g–$MoSe_2$ in the O_2-saturated electrolyte shows one ORR reduction peak at −0.15 V with a current density of 0.64 mA·cm^{-2}, whereas the ORR reduction peak for g–WSe_2 is at –0.21 V with a current density of 0.87 mA·cm^{-2}. These values approximate those of commercial Pt/C, which exists a cathodic peak potential of −0.12 V with a peak current density of 0.48 mA·cm^{-2} (Figure S7c). For comparison, the $MoSe_2$ and WSe_2 electrodes exhibit negatively shifted peak potentials at −0.19 V and −0.22 V, respectively, along with a considerably smaller peak current density (Figure S7).

To further study ORR performance, we carried out linear sweep voltammetry (LSV) measurements on an RDE for the $MoSe_2$, WSe_2, g–$MoSe_2$, g–WSe_2 electrodes, along with commercial Pt/C electrodes, in O_2-saturated 0.1 M KOH aqueous solution at a scan rate of 10 mV·s^{-1} and a rotation rate of 1600 rpm. As shown in Figure 7a, the onset potential for oxygen reduction at the $MoSe_2$ and WSe_2 electrodes is approximately –0.10 V, positively shifting to -0.02 V on g–$MoSe_2$ and g–WSe_2. The wide current plateau on g–$MoSe_2$ and g–WSe_2 was considered as the strong limiting diffusion current, indicating a diffusion-controlled process related to an efficient 4e$^-$ dominated ORR pathway.[35,50,51] The currents at –0.8 V for the $MoSe_2$, WSe_2, g–$MoSe_2$, g–WSe_2, and Pt/C electrodes are 3.44, 3.43, 5.35, 5.26, and 5.06 mA·cm^{-2}, respectively. The current values for the selenides and nanocomposite electrodes are approximately 68% and 105% that of the Pt/C, and these findings are consistent with the CV measurements. As evidenced by CV and LSV, the nanocomposite electrodes show favorable ORR catalytic activity, which is reflected by the positive onset potential and high current density. This result further confirms the significant contributions of single-layer graphene to ORR electrocatalytic activity.

To gain further insight into the kinetics of the composite-catalyzed ORR, we performed RDE measurement in an O_2-saturated 0.1 M KOH aqueous solution at various rotation speeds and a constant scan

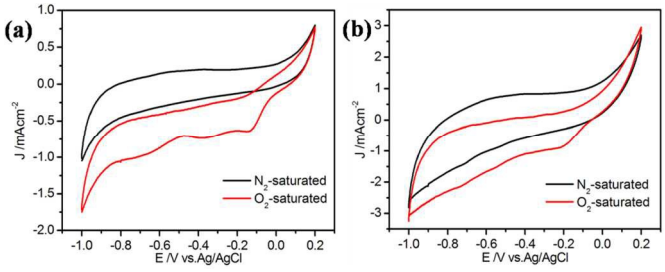

Figure 6 CV of (a) g–$MoSe_2$ (b) g–WSe_2 in N_2- and O_2-saturated 0.1M KOH solution at a scan rate of 10 mV·s^{-1}.

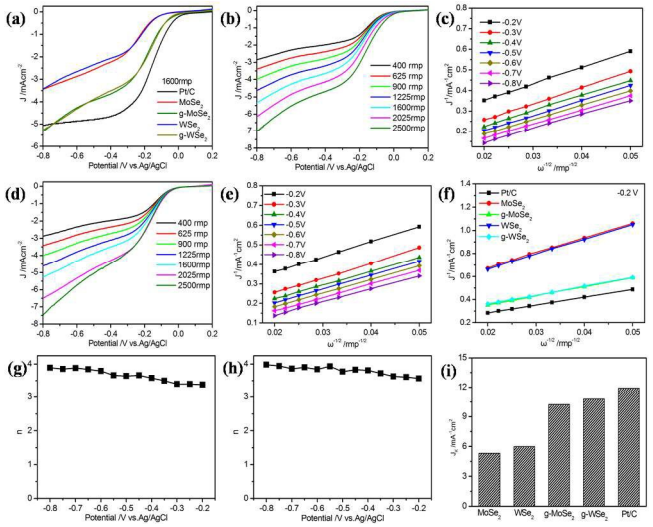

Figure 7 (a) Linear sweep voltammetry (LSV) of $MoSe_2$, WSe_2, g–$MoSe_2$, g–WSe_2, and Pt/C in O_2-saturated 0.1M KOH at a scan rate of 10 mVs^{-1} with an RDE rotation rate of 1600 rpm. (b, d) LSV of g–$MoSe_2$ and g–WSe_2 in O_2-saturated 0.1M KOH at a scan rate of 10 mVs^{-1} and at different RDE rotation rates. (c, e) Calculated K–L plots of the ORR from g–$MoSe_2$ and g–WSe_2. (f) K–L plots of the ORR from $MoSe_2$, WSe_2, g–$MoSe_2$, g–WSe_2, and Pt/C (g, h) Electron-transfer number n derived from K–L plots at different potentials. (i) Kinetic limiting current density (J_K) of $MoSe_2$, WSe_2, g–$MoSe_2$, g–WSe_2, and Pt/C.

rate of 10 mV·s^{-1}. As shown in Figures 7 and S8, the diffusion current densities increased with increasing rotating rates by shortened diffusion distance at high speeds, whereas the onset potentials remained virtually constant. The current densities for nanocomposite electrodes are considerably higher than those of selenides at any constant rotation rate. To quantitatively understand the ORR activity of the g–$MoSe_2$ and g–WSe_2 nanocomposites, we calculated the K–L plots from the LSVs for g–$MoSe_2$ and g–WSe_2 at various rotation speeds. Figures 7c and 7e show seven linear K–L plots at different potentials, suggesting that the inverse current density (1/j) is a function of the inverse of the square root of the rotation speed ($\omega^{-1/2}$) at different potential values and the first order reaction kinetics toward the concentration of O_2 on g–$MoSe_2$ and g–WSe_2 from −0.2 V to −0.8 V.[8] Figure 7f shows the K–L plots calculated from LSVs and compared at −0.2 V and at various rotation speeds. All K−L plots display good linearity. The oxygen reduction-involved electron transfer number per oxygen molecule (n) and kinetic limiting current density (J_K) can be calculated from the slope and the intercepts of the K–L equation (Figures 7g–7i). As shown in Figure S8i, the experimentally determined value (n=3.96) at the limiting potential of −0.2 V for commercial Pt/C agrees with the theoretically calculated value (n=4.0), indicating a four-electron oxygen reduction process. The corresponding numbers of electrons transferred per O_2 molecule at −0.2 V for $MoSe_2$, WSe_2, g–$MoSe_2$, and g–WSe_2 were calculated to be 2.10, 1.97, 3.40 and 3.57, respectively (Figures 7g, 7h and S8). The n values for selenide approximates a reduction process with a two-electron reaction pathway at −0.2 V.[52] By comparison, the ORR processes at the g–$MoSe_2$ and g–WSe_2 electrodes are markedly closer to a four-electron process. The g–$MoSe_2$ and g–WSe_2 electrodes show J_K

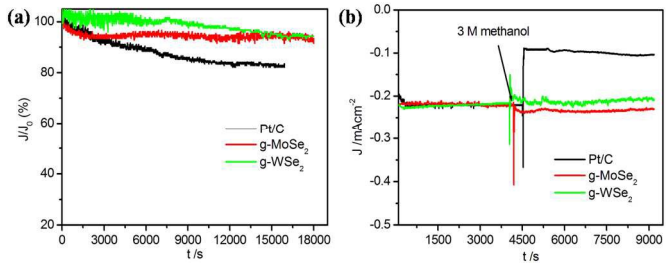

Figure 8 (a) Chronoamperometric response ($i - t$) of g–$MoSe_2$, g–WSe_2 and Pt/C, (b) $i - t$ of g–$MoSe_2$, g–WSe_2 and Pt/C before and after the addition of 3 M methanol. Tests were conducted in O_2-saturated 0.1 M KOH solution at −0.3V.

values of 10.22 and 10.77 mA·cm^{-2} at −0.2 V (close to that of commercial Pt/C, 11.91 mA·cm^{-2}), which are considerably higher than those of $MoSe_2$ (5.32 mA·cm^{-2}) and WSe_2 (5.99 mA·cm^{-2}). Evidently, the larger electron transfer number and the higher kinetic limiting current density further confirm the superior ORR performance of the g–$MoSe_2$ and g–WSe_2 composites. We also compared our catalysts with several recently reported non-noble metal catalysts that present outstanding performance for cathodic ORR (Supporting Information Table S2). In general, the performance of our g–$MoSe_2$ and g–WSe_2 catalysts is comparable with or is superior to those of the top reported catalysts in terms of peak potential, current density at −0.8V and *n*.

In addition to catalytic activity, stability and tolerance to methanol crossover are critical issues in fuel cell applications. To investigate the cycle stability of g–$MoSe_2$ and g–WSe_2 for ORR, we performed accelerated degradation testing by continuous chronoamperometric measurements at –0.3 V in an O_2-saturated 0.1 M KOH solution. The corresponding chronoamperometric response of the four catalysts and commercial Pt/C is shown in Figures 8a and S9. The current densities of all the electrodes initially decreased with time. However, the g–$MoSe_2$ and g–WSe_2 electrodes exhibit excellent stability with extremely slow decay rates, maintaining 91.5% and 94.3% of their initial currents even after 18,000 s, respectively, in comparison with the commercial Pt/C electrode at 82.8%. The $MoSe_2$ and WSe_2 electrodes also display slightly inferior stability, maintaining 84.5% and 85.6% of their initial currents (Figure S9). We speculated that the high stability of the two nanocomposites is mainly derived from the combination with rGO. The obvious aggregation did not occur in the catalytic process because of the interaction between rGO and selenides sheets driving from the thin layer structure. Thus, this ensured that the catalytic active sites on the catalyst surface were not significantly decreased, and the catalytic activity did not appear to be significantly reduced. These results indicate that these two nanocomposites exert considerably better electrochemical stability than the commercial Pt/C and selenides. Moreover, the g–$MoSe_2$, g–WSe_2, and commercial Pt/C catalysts were further compared by testing methanol crossover via chronoamperometric responses at the potential of −0.3 V (Figure 8b). A negative current appeared for O_2-saturated 0.1M KOH aqueous solution, indicating that the ORR occurred on g–$MoSe_2$, g–WSe_2, and Pt/C. A sharp decrease in ORR current density can be observed for the commercial Pt/C electrocatalyst upon the addition of methanol whereas the g–$MoSe_2$ and g–WSe_2 electrodes were insensitive to methanol. For a methanol fuel cell, methanol crossover from anode to cathode could diminish cathodic performance through the depolarizing effect. This measurement indicates that the g–$MoSe_2$ and g–WSe_2 catalysts possess excellent methanol tolerance, which is relevant in practical applications. Therefore, the atomically thin g–$MoSe_2$ and g–WSe_2 nanosheets developed in this work could be a promising electrocatalyst for the ORR in fuel cells. The ORR performance of the g-$MoSe_2$ and g-WSe_2 can be mainly attributed to the specific structure of ultrathin nanosheets (monolayer or double layer), which actually havemany active sites constructed by unsaturated chemical bonds. The purpose of combination with rGO is enhance the conductivity and construct favorable pore-structure, which finally can produce a good electrocatalyst for ORR.

4. Conclusions

In summary, atomically thin g–$MoSe_2$ and g–WSe_2 nanosheets were synthesize using an in situ, reductant–free solvothermal method and then tested as fuel cell cathode electrodes. The synthesized nanosheets exhibit remarkable electrocatalytic activities for ORR with higher tolerance to methanol crossover and longer-term stability than commercial Pt/C electrocatalysts. The electron transfer numbers for ORR on the atomically thin g–$MoSe_2$ and g–WSe_2 nanosheet catalysts are 3.89 and 3.98, respectively, indicating that a four-electron reduction pathway is favored. The excellent electrocatalytic activity of the nanocomposites profits from the ultrathin layer-by-layer structure, which promotes electrical conductivity, improves reactant adsorption and increases reactive site number. This study provides new insights and practical applications for designing atomically thin, ultrathin single-layer nanosheets as high-performance non-precious ORR electrocatalysts through low-cost and in situ synthesis techniques.

Acknowledgements

Financial support provided by the National Natural Science Foundation of China (Grant No. 51273032, 91333104, 51402036), International Science & Technology Cooperation Program of China (Grant No. 2013DFA51000), the Fundamental Research Funds for the Central Universities(Grant No. DUT15YQ109), and Natural Science Foundation of Anhui Province (Grant No. KJ2013A079). This research was also supported by the State Key Laboratory of Fine Chemicals of China.

Notes and references

[a] State Key laboratory of Fine Chemicals, School of Chemistry, Dalian University of Technology, Dalian, 116024, P. R. China.
E-mail: tinglima@dlut.edu.cn; shiyantao@dlut.edu.cn
[b] College of Chemistry and Materials Engineering, Anhui Science and Technology University, Fengyang, Anhui, 233100, P. R. China.
[c] School Petroleum and Chemical Engineering, Dalian University of Technology, Panjin Campus, Panjin 124221, P. R. China
[d] Graduate School of Life Science and Systems Engineering Kyushu Institute of Technology, Kitakyushu, Fukuoka, 808-0196, Japan

†Electronic Supplementary Information (ESI) available: SEM images of four catalyst; TEM, HRTEM, AFM images and XRD patterns of

$MoSe_2$ and WSe_2; O 1s core-level of nanocomposites; XPS spectra; CVs; LSVs; Chronoamperometric response; Percentages of different bindings of C 1s peak, Electrocatalytic performance of recently reported non-noble metal-based catalysts. See DOI: 10.1039/b000000x/

Reference

1 Y. Li, Q. Liu, W. Shen, *Dalton Trans.* **2011**, *40*, 5811.
2 K. Zhou, Y. Li, *Angew. Chem. Int. Ed.* **2012**, *51*, 602.
3 Y. Xiang, S. Lu and S. P. Jiang, *Chem. Soc. Rev.*, 2012, **41**, 7291.
4 C. Zhu and S. Dong, *Nanoscale,* 2013, **5**, 1753.
5 D. Wang, H. L. Xin, R. Hovden, H. Wang, Y. Yu, D. A. Muller, F. J. Disalvo, H. D. Abruña, *Nat. Mater.* 2013, **12**, 81.
6 Y. Liang, Y. Li, H. Wang and H. Dai, *J. Am. Chem. Soc.*, 2013, **135**, 2013.
7 G. Wu, K. L. More, C. M. Johnston, P. Zelenay, *Science*, 2011, **332**, 443.
8 S. J. Guo, S. Zhang, L. H. Wu, and S. H. Sun, *Angew. Chem.*, 2012, **124**, 11940.
9 R. Cao, J. S. Lee, M. Liu, J. Cho, *Adv. Energy Mater.,* 2012, **2** , 816.
10 J. Feng, X. Sun, C. Wu, L. Peng, C. Lin, S. Hu, J. Yang, Y. Xie, *J. Am. Chem. Soc.*, 2011, **133**, 17832.
11 K. S. Kim, Y. Zhao, H. Jang, S. Y. Lee, J. M. Kim, K. S. Kim, J. H. Ahn, P. Kim, J. Y. Choi, B. H. Hong, *Nature*, 2009, **457**, 706.
12 Q. Zheng, W. H. Ip, X. Lin, N. Yousefi, K. K. Yeung, Z. Li, J.K. Kim, *ACS Nano*, 2011, **5**, 6039.
13 Y. F. Sun, F. C. Lei, S. Gao, B. C. Pan, J. F. Zhou, and Y. Xie, *Angew. Chem. Int. Ed.*, 2013, **52**, 10569.
14 C. N. R. Rao, K. Gopalakrishnan, and U. Maitra, *ACS Appl. Mater. Interfaces,* 2015, **7**, 7809.
15 G. Eda, G. Fanchini, M. Chhowalla, *Nat. Nanotechnol.*, 2008, **3**, 270.
16 X. Li, G. Zhang, X. Bai, X. Sun, X. Wang, E. Wang, H. Dai, *Nat. Nanotechnol.*, 2008, **3**, 538.
17 X. Wang, L. Zhi, K. Mullen, *Nano Lett.*, 2007, **8**, 323.
18 H. Wang, G. Wang, P. Bao, S. Yang, W. Zhu, X. Xie, W. J. Zhang, *J. Am. Chem. Soc.*, 2012, **134**, 3627.
19 M. M. Liu, Y. Z. Lu, and W. Chen, *Adv. Funct. Mater.* 2013, **23**, 1289.
20 M. M. Liu, R. Z. Zhang, and W. Chen, *Chem. Rev.*, 2014, **114**, 5117.
21 R. Z. Zhang, and W. Chen, *J. Mater. Chem. A*, 2013, **1**, 11457.
22 Y. Z. Lu, Y. Y. Jiang and W. Chen, *Nanoscale*, 2014, **6**, 3309.
23 C. N. R. Rao, A. Nag, *Eur. J. Inorg. Chem.*, 2010, 2010, 4244.
24 L. F. Zhang and C. Y. Zhang, *Nanoscale*, 2014, **6**, 1782.
25 D. J. Zhao, S. Zhang, G. P. Yin, C. Y Du, Z. B. Wang, J. Wei, *J. Power Sources*, 2012, **206**, 103.
26 Y. J. Feng, T. He, and N. Alonso-Vante, *Fuel Cells*, 2010, **10**, 77.
27 H. T. Wang, D. S. Kong, Petr Johanes, Judy J. Cha, G. Y. Zheng, K. Yan, N. Liu, Y. Cui, *Nano Lett.*, 2013, **13**, 3426.
28 K. G. Zhou, N. N. Mao, H. X. Wang, Y. Peng, and H. L. Zhang, *Angew. Chem. Int. Ed.,* 2011, **50**, 10839.
29 J. H. Guo, Y. T. Shi, C. Zhu, L. Wang, N. Wang and T. L. Ma, *J. Mater. Chem. A,* 2013, **1**, 11874.
30 S. Wang, D. Yu, L. Dai, *J. Am. Chem. Soc.*, 2011, **133**, 5182.
31 S. Wang, D. Yu, L. Dai, D.W. Chang, J.-B. Baek, *ACS Nano*, 2011, **5**, 6202.
32 L. Y. Zhang, C. X. Guo, Z. Cui, J. Guo, Z. Dong, and C. M. Li, *Chem.–Eur. J.*, 2012, **18**, 15693.
33 D. Sun, S. M. Feng, M. Terrones, and R. E. Schaak, *Chem. Mater.*, 2015, **27**, 3167.
34 Y. F. Sun, F. C. Lei, S. Gao, B. C. Pan, J. F. Zhou, and Y. Xie, *Angew. Chem. Int. Ed.*, 2013, **52**, 10569.
35 X. D. Zhang, J. J. Zhang, J. Y. Zhao, B. C. Pan, M. G. Kong, J. Chen, and Y. Xie, *J. Am. Chem. Soc.,* 2012, **134**, 11908.
36 X. Lu, M. Iqbal Bakti Utama, J. H. Lin, X. Gong, J. Zhang, Y. Y. Zhao, Sokrates T. Pantelides, J. X. Wang, Z. L. Dong, Z. Liu, W. Zhou, and Q. H. Xiong, Nano Lett. 2014, 14, 2419−2425.
37 H. Fang, S. Chuang, T. C. Chang, K. Takei, T. Takahashi, and A. Javey, *Nano Lett.*, 2012, **12**, 3788.
38 W. Ai, Z. M. Luo, J. Jiang, J. H. Zhu, Z. Z. Du, Z. X. Fan, L. H. Xie, H. Zhang, W. Huang, and T. Yu, *Adv. Mater.,* 2014, **26**, 6186.
39 H. W. Zhou, Y. T. Shi, L. Wang, H. Zhang, C. Y. Zhao, A. Hagfeldt, and T. L. Ma, ***Chem. Commun.,***2013, **49**, 7626.
40 J. Kibsgaard, Z. Chen, B. N. Reinecke, T. F. Jaramillo, *Nat. Mater.*, 2012, **11(11)**, 963.
41 D. Merki, S. Fierro, H. Vrubel, X. Hu, *Chem. Sci.*, 2011, **2 (7),** 1262.
42 W. Abdallah, A. E. Nelson, *J. Mater. Sci.*, 2005, **40 (9−10)**, 2679.
43 J. D. Benck, Z. Chen, L. Y. Kuritzky, A. J. Forman, T. F. Jaramillo, *ACS Catal.,* 2012, **2 (9)**, 1916.
44 N. D. Boscher, C. J. Carmalt, I. P. Parkin, *J. Mater. Chem.,* 2006,**16 (1)**, 122.
45 H. T. Wang, D. S. Kong, P. Johanes, Judy J. Cha, G. Y. Zheng, K. Yan, N. Liu, and Y. Cui, *Nano Lett.*, 2013, **13**, 3426.
46 J. P. Zhao, S. F. Pei, W. C. Ren, L. B. Gao and H. M. Cheng, *ACS Nano*, 2010, **4**, 5245.
47 H. X. Tang, G. J. Ehlert, Y. R. Lin and H. A. Sodano, *Nano Lett.*, 2012, **12**, 84.
48 Z. X. Jiang, J. J. Wang, L. H. Meng, Y. D. Huang and L. Liu, *Chem. Commun.*, 2011, **47**, 6350.
49 S. Stankovich, D. A. Dikin, R. D. Piner, K. A. Kohlhaas, A. Kleinhammes, Y. Jia, Y. Wu, S. T. Nguyen and R. S. Ruoff, *Carbon*, 2007, **45**, 1558.
50 Y. Zheng, Y. Jiao, J. Chen, J. Liu, J. Liang, A. J. Du, W. M. Zhang, Z. H. Zhu, S. C. Smith, M. Jaroniec, G. Q. (Max) Lu, and S. Z. Qiao, *J. Am.Chem. Soc.,* 2011, **133**, 20116.
51 J. J. Duan, S. Chen, S. Dai, and S. Z. Qiao, *Adv. Funct. Mater.,* 2014, **24**, 2072.
52 H. S. Wroblowa, P. Yen Chi, G. Razumney, *J. Electroanal. Chem. Interfacial Electrochem.,* 1976, **69**, 195.

Atomically Thin $MoSe_2$/graphene and WSe_2/ graphene Nanosheets for Highly Efficient Oxygen Reduction Reaction

JiahaoGuo,[a,b] Yantao Shi,[a,*] Xiaogong Bai,[a] Xuchun Wang,[b] and Tingli Ma [c,d*]

[a]State Key laboratory of Fine Chemicals, School of Chemistry, Dalian University of Technology, Dalian, 116024, China. E-mail: tinglima@dlut.edu.cn; shiyantao@dlut.edu.cn

[b]College of Chemistry and Materials Engineering, Anhui Science and Technology University, Fengyang, 233100, China.

[c] School Petroleum and Chemical Engineering, Dalian University of Technology, Panjin Campus, Panjin 124221, China

[d]Graduate School of Life Science and Systems Engineering, Kyushu Institute of Technology, Kitakyushu, Fukuoka, 808-0196, Japan

Atomically thin g-$MoSe_2$ and g-WSe_2 nanosheets have successfully realized in situ growth on reduced graphene oxide. These two nanocomposites possessed mesoporous structures that facilitate oxygen adsorption and moss transport during the ORR. Compared with $MoSe_2$ and WSe_2, the nanocomposites possess prominent ORR catalytic activity, closely approximating that of commercial Pt/C. The two nanocomposites also exhibited outstanding fuel crossover resistance and stronger durability in alkaline media. The ORR processes at the g–$MoSe_2$ and g–WSe_2 electrodes are markedly closer to an ideal four-electron process. This study provides new insights and practical applications for designing atomically thin single-layer IGAs nanosheets as high-performance non-precious ORR electrocatalysts.